Zhu et al. *Zool. Res.* 2024, 45(4): 937−950
https://doi.org/10.24272/j.issn.2095-8137.2024.021

ZR | Zoological Research

Article Open Access

TAX1BP1 and FIP200 orchestrate non-canonical autophagy of p62 aggregates for mouse neural stem cell maintenance

Yi-Fu Zhu[1,#], Rong-Hua Yu[2,#], Shuai Zhou[2], Pei-Pei Tang[3], Rui Zhang[2], Yu-Xin Wu[2], Ran Xu[6], Jia-Ming Wei[3], Ying-Ying Wang[2], Jia-Li Zhang[2], Meng-Ke Li[2], Xiao-Jing Shi[4], Yu-Wei Zhang[5], Guang-Zhi Liu[5], Rick F. Thorne[2], Xu Dong Zhang[2,6], Mian Wu[1,2,5,*], Song Chen[2,3,5,*]

[1] *School of Life Sciences*, *Division of Life Sciences and Medicine*, *University of Science and Technology of China*, *Hefei*, *Anhui* 230001, *China*

[2] *Translational Research Institute of Henan Provincial People's Hospital and People''s Hospital of Zhengzhou University*, *Tianjian Laboratory of Advanced Biomedical Sciences*, *Academy of Medical Sciences*, *Zhengzhou University*, *Zhengzhou*, *Henan* 450053, *China*

[3] *Institute of Medicinal Biotechnology*, *Jiangsu College of Nursing*, *Huai'an*, *Jiangsu* 223300, *China*

[4] *Laboratory Animal Center*, *Academy of Medical Science*, *Zhengzhou University*, *Zhengzhou*, *Henan* 450052, *China*

[5] *Henan Key Laboratory of Stem cell Differentiation and Modification*, *Henan Provincial People's Hospital*, *Henan University*, *Zhengzhou*, *Henan* 450053, *China*

[6] *School of Biomedical Sciences and Pharmacy*, *The University of Newcastle*, *NSW* 2308, *Australia*

ABSTRACT

Autophagy plays a pivotal role in diverse biological processes, including the maintenance and differentiation of neural stem cells (NSCs). Interestingly, while complete deletion of *Fip200* severely impairs NSC maintenance and differentiation, inhibiting canonical autophagy via deletion of core genes, such as *Atg5*, *Atg16l1*, and *Atg7*, or blockade of canonical interactions between FIP200 and ATG13 (designated as FIP200-4A mutant or FIP200 KI) does not produce comparable detrimental effects. This highlights the likely critical involvement of the non-canonical functions of FIP200, the mechanisms of which have remained elusive. Here, utilizing genetic mouse models, we demonstrated that FIP200 mediates non-canonical autophagic degradation of p62/sequestome1, primarily via TAX1BP1 in NSCs. Conditional deletion of *Tax1bp1* in *fip200*^{hGFAP} conditional knock-in (cKI) mice led to NSC deficiency, resembling the *fip200*^{hGFAP} conditional knockout (cKO) mouse phenotype. Notably, reintroducing wild-type TAX1BP1 not only restored the maintenance of NSCs derived from *tax1bp1*-knockout *fip200*^{hGFAP} cKI mice but also led to a marked reduction in p62 aggregate accumulation. Conversely, a TAX1BP1 mutant incapable of binding to FIP200 or NBR1/p62 failed to achieve this restoration. Furthermore, conditional deletion of *Tax1bp1* in *fip200*^{hGFAP} cKO mice exacerbated NSC deficiency and p62 aggregate accumulation compared to *fip200*^{hGFAP} cKO mice. Collectively, these findings illustrate the essential role of the FIP200-TAX1BP1 axis in mediating the non-canonical autophagic degradation of p62 aggregates towards NSC maintenance and function, presenting novel therapeutic targets for neurodegenerative diseases.

Keywords: Non-canonical autophagy; TAX1BP1; FIP200; p62; Aggregates; Neural stem cell

INTRODUCTION

Neurogenesis, responsible for producing all neuronal lineages in the central nervous system (CNS) —including neurons, astrocytes, and oligodendrocytes —is primarily active during development but persists into adulthood to maintain tissue homeostasis. Analogous to hematopoiesis, neurogenesis constitutes a hierarchical differentiation cascade involving multipotent progenitors termed neural stem cells (NSCs) (Casares-Crespo et al., 2018; Fleming & Rubinsztein, 2020; Zhao et al., 2008). Rodent research has established that adult neurogenesis occurs in the subventricular zone (SVZ) of the lateral ventricle and within the dentate gyrus (DG) subgranular zone (SGZ) of the hippocampus (Doetsch et al., 1999; Gage, 2000; Palmer et al., 1997). However, the debate on whether adult NSCs have specific locational functions persists (Becher & Holland, 2010), with some studies suggesting that adult

Received: 22 January 2024; Accepted: 30 April 2024; Online: 01 May 2024

Foundation items: This work was supported by the National Natural Science Foundation of China (U2004138, 81773132, 81820108021), University Excellent Teaching Team of "Qinglan Project" in Jiangsu Province (2022-25), Henan Province Key Research and Development Project (232102521028), and Excellent Youth Foundation of Henan Scientific Committee (21230040016)

[#]Authors contributed equally to this work

*Corresponding authors, E-mail: wumian@ustc.edu.cn; schen@zzu.edu.cn

neurogenesis contributes to olfaction in the SVZ but to learning and memory in the hippocampus (Liu et al., 2013). Disruptions in NSC maintenance and neurogenesis can contribute to developmental abnormalities and neurodegenerative conditions, such as Alzheimer's, Parkinson's, and Huntington's diseases (Huang & Klionsky, 2007). Thus, elucidating the cellular and molecular mechanisms governing NSC functionality could pave the way for novel therapeutic interventions.

Autophagy is a highly conserved degradation pathway essential for the removal of damaged organelles and protein aggregates. This lysosome-dependent process is critical in the etiology of various diseases, including neurodegeneration, cancer, and autoimmunity (Guo & Zhao, 2020; Klionsky et al., 2021; Thorburn, 2018). Canonical autophagy, orchestrated by autophagy-related genes (ATGs), is crucial for the initiation and maturation of autophagosomes to facilitate degradation (Bhutia et al., 2018). Notably, while deletion of canonical ATGs in neuronal lineages, such as *Atg5*, *Atg7*, and *Atg16l1*, results in protein aggregate accumulation and subsequent neurodegeneration, these manipulations do not influence NSC maintenance or differentiation (Donde et al., 2020; Liang et al., 2010; Vázquez et al., 2012; Wang et al., 2014; Xi et al., 2016). Similarly, deletion of the autophagy activator protein *Fip200/Rb1cc1* (RB1 inducible coiled-coil 1) in the central and peripheral nervous system leads to characteristic neuropathies, including progressive axonopathy and spongiform degeneration associated with the accumulation of ubiquitinated protein aggregates (Liang et al., 2010). However, subsequent studies have demonstrated that eliminating FIP200 expression severely impacts NSC homeostasis through the progressive depletion of NSCs (Wang et al., 2013, 2016). These contrasting observations provide valuable insights into the potential mechanisms regulating NSC fitness during adult neurogenesis.

FIP200 is traditionally recognized for initiating canonical autophagy through complex formation with ATG13-ULK1-ATG101. However, research has revealed that FIP200 has more expansive roles, interacting with a range of autophagy-related proteins such as calcium binding and coiled-coil domain 2 (CALCOCO2/NDP52), cell cycle progression 1 (CCPG1), 5-azacytidine induced 2 (AZI2/NAP1), and sequestome1 (SQSTM1/p62) and key regulators such as p53 and TSC complex subunit 1 (TSC1), thereby modulating diverse cellular functions via non-canonical autophagy (Yeo et al., 2020). As a multifunctional adaptor protein, p62 acts as a major receptor for the degradation of ubiquitinated protein aggregates (Bjørkøy et al., 2006; Lyu et al., 2022; Pankiv et al., 2007). Deletion and mutations in p62 are associated with neurodegenerative diseases such as Alzheimer's disease (Schaeffer & Goedert, 2012; Zheng et al., 2012), Parkinson's disease (Friesen et al., 2020; Oh et al., 2022), Huntington's disease (Rué et al., 2013; Yang et al., 2021), amyotrophic lateral sclerosis (ALS) (Majcher et al., 2015), and frontotemporal lobar degeneration (FTLD) (Deng et al., 2020; Ma et al., 2019). Notably, p62 was the first selective autophagy receptor implicated in macroautophagy (also termed aggrephagy) (Bjørkøy et al., 2006; Pankiv et al., 2007). Subsequent research has identified several other aggrephagy receptors, including next to BRCA1 gene 1 protein (NBR1), nuclear dot protein 52 (NDP52), optineurin (OPTN), tax1 binding protein 1 (TAX1BP1), toll interacting protein (TOLLIP), and chaperonin containing TCP1 subunit 2 (CCT2) (Gibertini et al., 2023; Ma et al., 2022; Sarraf et al., 2020; Trapannone et al., 2023). Despite these discoveries, the function of aggrephagy in NSCs remains unclear. We previously showed that *Fip200* deletion in NSCs, but not knockout of *Atg5*, *Atg7*, or *Atg16l1*, leads to the accumulation of p62, NBR1, and TAX1BP1 along with p62/ubiquitinated protein aggregates (Wang et al., 2016). Of note, deletion of *p62* rescues *fip200*^{hGFAP} conditional knockout (cKO) NSCs, highlighting the pivotal role of aggrephagy in NSC maintenance and neurogenesis (Gibertini et al., 2023; Ma et al., 2022; Sarraf et al., 2020; Trapannone et al., 2023).

Here, we elucidated the discrete functions of three aggrephagy receptors —TAX1BP1, p62, and NBR1 —during NSC maintenance using a mouse model with conditional gene deletions in NSCs and reconstitution with functionally deficient mutants. Similar to *fip200*^{hGFAP} cKO mice, conditional deletion of *Tax1bp1* in *fip200* conditional knock-in (cKI) mice resulted in the aggregation of NBR1 and p62, resulting in NSC deficiency. Conditional deletion of *Tax1bp1* in *fip200* cKO mice exacerbated p62/NBR1 aggregation and NSC deficiency compared to *fip200* cKO mice. Identification of the underlying non-canonical autophagic mechanism indicated that NBR1 promotes interactions between TAX1BP1 and p62 aggregates. Overall, our study revealed a mechanism by which FIP200 regulates NSC maintenance and differentiation via non-canonical autophagy of p62/aggregates, principally via TAX1BP1.

MATERIALS AND METHODS

Mouse experiments

The *fip200* cKO mice, with *Fip200* conditionally deleted in postnatal NSCs (Wang et al., 2013, 2016), were generated by crossing *hGFAP*-Cre transgenic mice, expressing Cre in postnatal NSCs (Wang et al., 2009, 2013), with *fip200* F/F mice. The *fip200* cKI mice, carrying *fip200* F/KI alleles (Chen et al., 2016), were crossed with *hGFAP*-Cre mice. The *tax1bp1* F/F mice, bearing two flox alleles with exon 4 flanked by two loxP sequences, were newly generated. The *tax1bp1* cKO mice, carrying *tax1bp1* F/F alleles, were crossed with *hGFAP*-Cre mice. The *fip200* cKI; *tax1bp1* cKO mice, carrying *fip200* F/KI and *tax1bp1* F/F alleles, were crossed with *hGFAP*-Cre mice. The *fip200* cKO; *tax1bp1* cKO (*2* cKO) mice, carrying the *fip200* F/F and *tax1bp1* F/F alleles, were crossed with *hGFAP*-Cre mice. All mice were maintained on FVB backgrounds. Age- and littermate-matched control and mutant mice were used for analysis to minimize the impact of modifier genes. All animal experiments and procedures were carried out in accordance with the guidelines of the Institutional Animal Care and were approved by Animal Research Ethics Committee of the Laboratory Animal Center of Zhengzhou University (ZZU-LAC20210702[17]). Genotyping for *Fip200* F/F, *Fip200* +/KI, *Tax1bp1* F/F, and *Cre* alleles was performed by polymerase chain reaction (PCR) analysis of tail DNA.

Reagents and antibodies

Plasmid transfections were carried out using Lipo8000 transfection reagent (Beyotime, China). Small interfering RNA (siRNA) transfections were carried out using Lipofectamine RNAiMAX transfection reagent (Invitrogen, USA).

Primary antibodies included mouse anti-b-ACTIN (Sigma, USA, 1:5 000 dilution), rabbit anti-FIP200 (Proteintech, China, 1:2 000 dilution), rabbit anti-p62 (Cell Signaling Technology,

USA, 1:1 000 dilution), mouse anti-NBR1 (Santa Cru Biotechnology, USA, 1:500 dilution), rabbit anti-TAX1BP1 (Proteintech, China, 1:1 000 dilution), rabbit anti-OPTN (Proteintech, China, 1:1 000 dilution), rabbit anti-TOLLIP (Proteintech, China, 1:1 000 dilution), rabbit anti-CCT2 (Proteintech, China, 1:1 000 dilution), mouse anti-HA (Sigma, USA , 1:5 000 dilution), mouse anti-Flag (Sigma, USA, 1:5 000 dilution), mouse anti-GFP (Santa Cru Biotechnology, USA, 1:1 000 dilution), mouse anti-GFAP (Proteintech, China, 1:1 000 dilution), rabbit anti-NESTIN (Proteintech, China, 1:1 000 dilution), rabbit anti-SOX2 (Proteintech, China, 1:1 000 dilution), rabbit anti-DOUBLECORTIN (Servicebio, China, 1:1 000 dilution), rabbit anti-KI67 (Servicebio, China, 1:1 000 dilution). Secondary antibodies included goat anti-rabbit IgG (H+L), horseradish peroxidase (HRP) (Invitrogen, USA, 1:50 000 dilution), goat anti-mouse IgG (H+L) horseradish peroxidase (HRP) (Invitrogen, USA, 1:50 000 dilution), chicken anti-mouse IgG (H+L) cross-adsorbed, Alexa Fluor 488 (Invitrogen, USA, 1:1 000 dilution), goat anti-rabbit IgG (H+L) cross-adsorbed, and Alexa Fluor 594 (Invitrogen, USA, 1:1 000 dilution).

Cell culture and treatment

Mouse SVZ tissues at postnatal day 0 (P0) and P28 were isolated under a dissection microscope and cut into 1 mm^3 cubes. The tissues were digested in 0.2% trypsin to obtain single-cell suspensions. The cells were cultured in neurobasal medium (Gibco, USA) supplemented with B27 without vitamin A (Gibco, USA), 10 ng/mL basic fibroblast growth factor (bFGF, Novoprotein, China), and 20 ng/mL epidermal growth factor (EGF, Novoprotein, China) in ultra-low attachment multiple well plates (Corning, USA). The medium was supplemented on days 3, 6, and 9. Neurospheres with diameters larger than 50 μm were counted 9 d after culturing. For passaging, primary neurospheres were collected and incubated in 0.2% trypsin at 37°C for 10 min with pipetting 50 times. After the addition of trypsin inhibitor (Sigma, Germany) supplemented with DNase I (Beyotime, China) to stop digestion, dispersed cells were collected by centrifugation at 400 ×*g* for 10 min at room temperature, counted and cultured for secondary neurosphere formation, with quantification conducted in the same way as primary neurosphere formation. HEK293T cells (ATCC) were cultured in Dulbecco's Modified Eagle Medium (DMEM) supplemented with 10% fetal bovine serum (FBS), L-glutamine (2 mmol/L), penicillin (10 Units/mL), and streptomycin (0.1 mg/mL).

For siRNA treatment, NSCs were seeded in 24-well plates (100 000 cells/well). After 24 h, the cells were transfected with siRNA (25 nmol/L final concentration) using Lipofectamine™ RNAiMAX transfection reagent in OptiMEM medium. At 8 h after transfection, the NSCs were cultured in 6-well plates (20 000 cells/well) for 5 days. The siRNA sequences were: Tax1bp1, 5'-GUCUCCUAUGCCUGAACAU-3'; Nbr1, 5'-GCCACUUGCACAUUAUUCU-3'; and p62, 5'-GCUGAAACAUGGACACUUU-3'.

Stable expression of full-length or mutant forms of TAX1BP1 was achieved using lentiviral-mediated transduction. The indicated epitope-tagged constructs were cloned into the Lenti-EFS-Flag-puro vector and transfected with psPAX2 and pmd2.g in HEK293T cells to derive lentiviral particles. After centrifugation at 3 000 ×*g* for 10 min at room temperature and filtration through 0.45 μm filter (Beyotime, China), lentiviral supernatants were added to NSCs. The infected neurospheres were selected with 1 μg/mL puromycin in neurosphere media to obtain pools stably expressing Tax1bp1 mutants.

Western blotting

Mouse SVZ tissues were microdissected from brains and extracted in sodium dodecyl sulfate (SDS)-lysis buffer containing 2% SDS, 62.5 mmol/L Tris pH 6.8, 10% glycerol, and 5% β-mercaptoethanol.

Lysates were boiled for 10 min and analyzed by sodium dodecyl-sulfate polyacrylamide gel electrophoresis (SDS-PAGE) on 4%–20% gels (160 V, 45 min) (BioRad Laboratories, USA), followed by immunoblotting on nitrocellulose membranes using a wet blotting system (400 mA, 30 min) (BioRad Laboratories, USA). Membranes were incubated with primary and secondary antibodies diluted in 5% milk/TBST solutions, and immunocomplexes were developed using SuperSignal™ West Pico PLUS (Thermo Fisher, USA) and visualized using an Azure c600 Western Blot Imager (Azure Biosystems, USA).

Immunoprecipitation

At 24 h post-transfection, HEK293FT cells were lysed in immunoprecipitation buffer (50 mmol/L Tris-HCl, pH 8.0, 150 mmol/L NaCl, 0.5 mmol/L ethylenediaminetetraacetic acid (EDTA), 0.5% NP-40, 10% glycerol) containing EDTA-free protease inhibitor cocktail (MCE, China) for 30 min at 4°C. The lysates were centrifuged at 12 000 ×*g* for 10 min at 4°C, and the soluble supernatant fractions were subjected to immunoprecipitation with Pierce™Anti-DYKDDDDK Magnetic Agarose (Invitrogen, USA) or Pierce Anti-HA Magnetic Beads (Invitrogen, USA). After incubation for 4 h at 4°C, the beads were washed three times with TBST and boiled with SDS-lysis buffer for 10 min.

Histology and immunofluorescence

Mice were euthanized using CO_2, and whole brains were collected after perfusion. Fixation was performed for 16 h at 4°C using 4% (wt/vol) freshly made, prechilled phosphate-buffered saline (PBS)-buffered paraformaldehyde (PFA). Brain tissues were sagittally sectioned, embedded in paraffin, and cut into 5 μm slices using a Leica 2125 Microtome (Leica, Germany). Slides from histologically comparable positions (triangular lateral ventricle with intact rostral migratory stream (RMS)) were subjected to hematoxylin and eosin (H&E) and immunofluorescence (IF) staining. For routine histological examination, sections were stained with H&E. For IF analysis of brain tissue, sections were washed in xylene three times (5 min each), rehydrated in graded ethanol solutions (100%, 95%, 85%, and 75%, 2 min each). After heat-activated antigen retrieval in Tris-EDTA pH 9.0 buffer, 6% bovine serum albumin (BSA)/TBST solution was used to block the sections at room temperature for 30 min. Sections were incubated with primary antibodies at 4°C for 16 h in an immunohistochemical wet box, washed in PBS three times (5 min each), and incubated with 1:1 000 Alexa Fluor™ 488 or Alexa Fluor™ 594 secondary antibodies for 1 h at room temperature. After washing three times (5 min each) in PBS, sections were stained with antifade mounting medium with 4',6-diamidino-2-phenylindole (DAPI, Beyotime, China) and visualized using epifluorescence or confocal microscopy (Nikon, Japan). For IF, NSCs were fixed in cold methanol for 10 min, blocked in 3% BSA/TBST solution for 30 min, then incubated with primary and secondary antibodies as described as above.

Statistical analysis

Statistical significance was determined using GraphPad Prism v.6, using unpaired Student's two-tailed *t*-test for one-way comparisons and one-way analysis of variance (ANOVA) for multiple comparisons. No statistical methods were used to determine sample sizes. Unless expressly noted, experiments were not randomized, and the investigators were not blinded to group allocations or outcome assessments. Data are presented as mean±standard error of the mean (SEM) (error bars). *: $P<0.05$; **: $P<0.01$; ***: $P<0.001$; and ****: $P<0.0001$.

RESULTS

Self-renewal of *fip200* cKI NSCs *in vitro* is impaired by *TAX1BP1* knockdown

Prior studies have demonstrated that reconstitution of *fip200* KO mice with an ATG13-binding mutant, denoted FIP200-4A (Chen et al., 2016), is sufficient to sustain murine NSC maintenance and neurogenesis *in vivo* (Liu et al., 2021). However, the specific mechanisms by which the FIP200-4A mutant supports NSC homeostasis in the context of the *fip200* KI mice remain unclear.

To further explore this paradigm, we generated *fip200* cKO mice and *fip200* cKI mice. By P28, the *fip200* cKI mice exhibited normal physical development and hindlimb motor abilities compared to the *fip200* cKO mice (Supplementary Figure S1A, B). Consistent with earlier research (Liu et al., 2021), histological analysis revealed that *fip200* cKI mice displayed restored SVZ cellularity and DG area measures compared to the *fip200* cKO mice (Supplementary Figure S1C, D). Additionally, a marked accumulation of p62 was observed in the SVZ and DG of *fip200* cKO mice, but not in wild-type (WT) or *fip200* cKI mice (Figure 1A; Supplementary Figure S1E). The presence of unresolved p62 aggregates suggests that differences between the *fip200* cKO and *fip200* cKI mice involve disruptions in NSC maintenance resulting from defective non-canonical autophagy of protein aggregates (or aggrephagy).

In addition to p62, previous studies have reported the accumulation of autophagy receptors TAX1BP1 and NBR1 in *fip200*^{hGFAP} cKO NSCs (Wang et al., 2016), necessitating the identification of specific aggrephagy receptors utilized in NSCs. To gain further mechanistic insights, we evaluated six reported aggrephagy receptors —TAX1BP1, NBR1, p62, OPTN, TOLLIP, and CCT2—in SVZ tissues of different *Fip200* genotypes. Western blotting revealed significant elevations in the TAX1BP1, NBR1, and p62 protein levels in *fip200* cKO mice, while the levels of OPTN, TOLLIP, and CCT2 showed no detectable changes (Figure 1B; Supplementary Figure S1F). Consistent with these *in vivo* observations, the protein levels of TAX1BP1, NBR1, and p62 were significantly increased in *fip200* cKO NSCs (Figure 1C; Supplementary Figure S1G).

To explore functional relationships, TAX1BP1, NBR1, and p62 were knocked down in P28-derived NSCs from different experimental backgrounds. Depleting TAX1BP1 led to a significant increase in p62 and NBR1 protein levels in *fip200* cKI NSCs but not in *fip200* cKO NSCs. In contrast, NBR1 knockdown did not significantly affect TAX1BP1 or p62 levels (Figure 1D; Supplementary Figure S1H). Neurosphere assays used to assess NSC self-renewal showed that individual knockdown of TAX1BP1, NBR1, and p62 did not impact the self-renewal capacity of WT NSCs. However, p62 knockdown largely restored the diminished self-renewal capability of *fip200* cKO NSCs. In contrast, TAX1BP1 knockdown further reduced neurosphere formation in *fip200* cKO NSCs, with similar impairment observed in *fip200* cKI NSCs. NBR1 knockdown exerted negligible effects on *fip200* cKO NSCs, with only a modest reduction in neurosphere formation observed in *fip200* cKI NSCs (Figure 1E, F). Strikingly, similar to *fip200* cKO NSCs, TAX1BP1 knockdown led to a significant accumulation of p62 aggregates in *fip200* cKI NSCs (Figure 1G, H). These results suggest that the degradation of p62 aggregates via the FIP200-4A mutant primarily relies on TAX1BP1 as an essential intermediary, with its loss inducing p62 aggregate accumulation in NSCs (Figure 1I).

TAX1BP1 ablation in *fip200* cKI mice causes SVZ degeneration via NSC deficiency

To further investigate the role of TAX1BP1 in maintaining NSC homeostasis *in vivo*, we generated cKO mice with exon 4 of the *Tax1bp1* allele flanked by loxP sites. These mice were crossed with *hGFAP*-Cre transgenic mice to produce NSC-specific *tax1bp1* cKO mice (Supplementary Figure S2A-D). Founder mice were also used to generate *tax1bp1* cKO mice on a *fip200* cKI background (*fip200* cKI; *tax1bp1* cKO mice).

Initial evaluation of SVZ tissues at P28 among the genotypes showed a significant increase in p62 protein levels in the *fip200* cKI; *tax1bp1* cKO mice relative to their WT, *fip200* cKI, and *tax1bp1* cKO littermates (Figure 2A; Supplementary Figure S2E), suggesting considerable blockade of p62 aggregate degradation. Neurosphere assays confirmed marked reductions in neurosphere formation in both primary and secondary SVZ cultures derived from P28 *fip200* cKI; *tax1bp1* cKO mice (Figure 2B, C). H&E staining showed significant reductions in both SVZ and DG width and cellularity in *fip200* cKI; *tax1bp1* cKO mice, whereas these parameters in *fip200* cKI and *tax1bp1* cKO mice were similar to those in WT mice (Figure 2D, E). These phenotypes, together with the *in vitro* results, imply that TAX1BP1 is necessary to maintain normal NSCs in *fip200* cKI mice.

To conclusively establish the role of TAX1BP1, we analyzed the NSC populations in the SVZ and DG using GFAP^{+}NESTIN^{+} and GFAP^{+}SOX2^{+} markers. Results revealed significant reductions in the NSC population in *fip200* cKI; *tax1bp1* cKO mice compared to their *fip200* cKI and *tax1bp1* cKO counterparts (Figure 2F–I; Supplementary Figure S2F–I). Furthermore, *fip200* cKI; *tax1bp1* cKO mice exhibited decreased proliferation and differentiation and increased apoptosis and microglial infiltration (Figure 2J–M; Supplementary Figure S2J–O). These findings underscore the critical role of TAX1BP1 in the maintenance and differentiation of postnatal NSCs in *fip200* cKI mice.

TAX1BP1 ablation in *fip200* cKI mice leads to NSC deficiency through p62/NBR1 aggregation

Given that TAX1BP1 ablation increased p62 levels in the SVZ of *fip200* cKI mice, we next investigated its involvement in the formation of p62/NBR1 aggregates and consequent impact on the NSC pool. We first explored how manipulating TAX1BP1 affected NBR1 and p62 protein levels in SVZ tissues across different experimental backgrounds. Results showed a marked up-regulation of NBR1 and p62 in the SVZ of *fip200* cKI; *tax1bp1* cKO mice, while their levels in *fip200* cKI and *tax1bp1* cKO mice remained comparable to that in WT mice (Figure 3A; Supplementary Figure S3A). Moreover, increased NBR1 and p62 aggregates were found in the SVZ and DG regions of *fip200* cKI; *tax1bp1* cKO mice (Figure 3B-E),

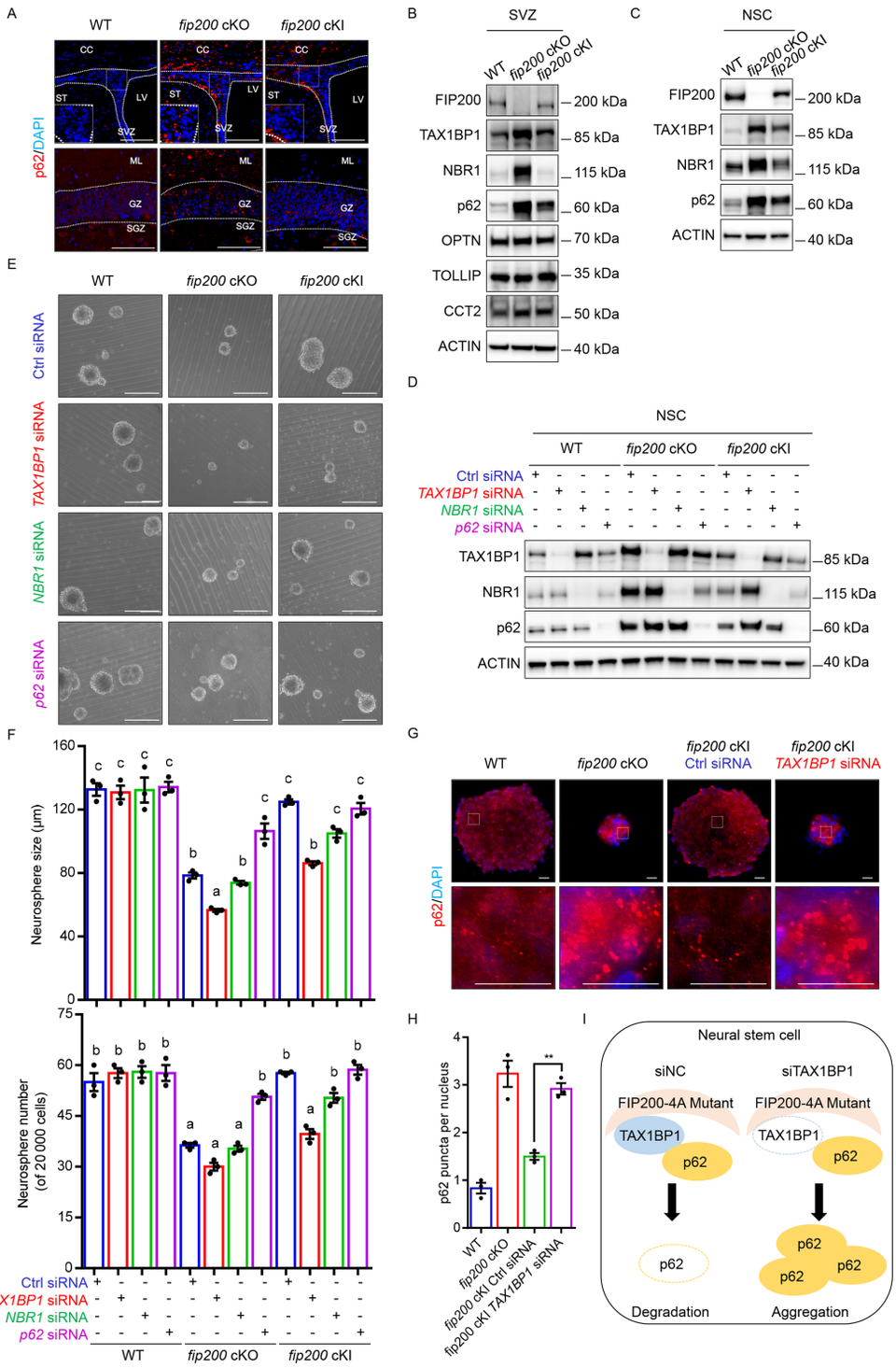

Figure 1 Sufficient self-renewal of *fip200* cKI NSCs *in vitro* is impaired by TAX1BP1 knockdown

A: Immunofluorescence of p62 puncta and DAPI in SVZ and SGZ from WT, *fip200* cKO, *fip200* cKI mice at P28. Dotted lines indicate boundaries of SVZ and DG. Scale bar: 100 μm. B: Lysates were extracted from the SVZ of P28 WT, *fip200* cKO, and *fip200* cKI mice, with aggrephagy receptor protein levels analyzed by western blotting. ACTIN was used as a loading control. C: Lysates were extracted from NSCs of P28 WT, *fip200* cKO, and *fip200* cKI mice, with TAX1BP1, NBR1, and p62 protein levels analyzed by western blotting. ACTIN was used as a loading control. D: Western blotting of FIP200, TAX1BP1, NBR1, and p62 protein levels in WT, *fip200* cKO, and *fip200* cKI NSCs with or without *TAX1BP1*, *NBR1*, or *p62* siRNA transfection. ACTIN was used as a loading control. E: Neurosphere formation from WT, *fip200* cKO, and *fip200* cKI NSCs with or without *TAX1BP1*, *NBR1* or *p62* siRNA transfection. Representative phase contrast images. Scale bar: 200 μm. F: Mean±SEM of number and size of neurospheres (n=3 independent samples). Same character means not significant, different character means P<0.05 (one-way ANOVA with Tukey's multiple comparisons test). G: Immunofluorescence of p62 puncta and DAPI in WT, *fip200* cKO, *fip200* cKI Ctrl siRNA, and *fip200* cKI *TAX1BP1* siRNA neurospheres. Scale bar: 20 μm. H: Mean±SEM of p62 puncta per neurosphere (n=3 independent samples). **: P<0.01 (one-way ANOVA with Dunnett's multiple comparisons test). I: Schematic of FIP200 4A-mutant, TAX1BP1 and p62 status in Ctrl siRNA or *TAX1BP1* siRNA *fip200* cKI NSC conditions.

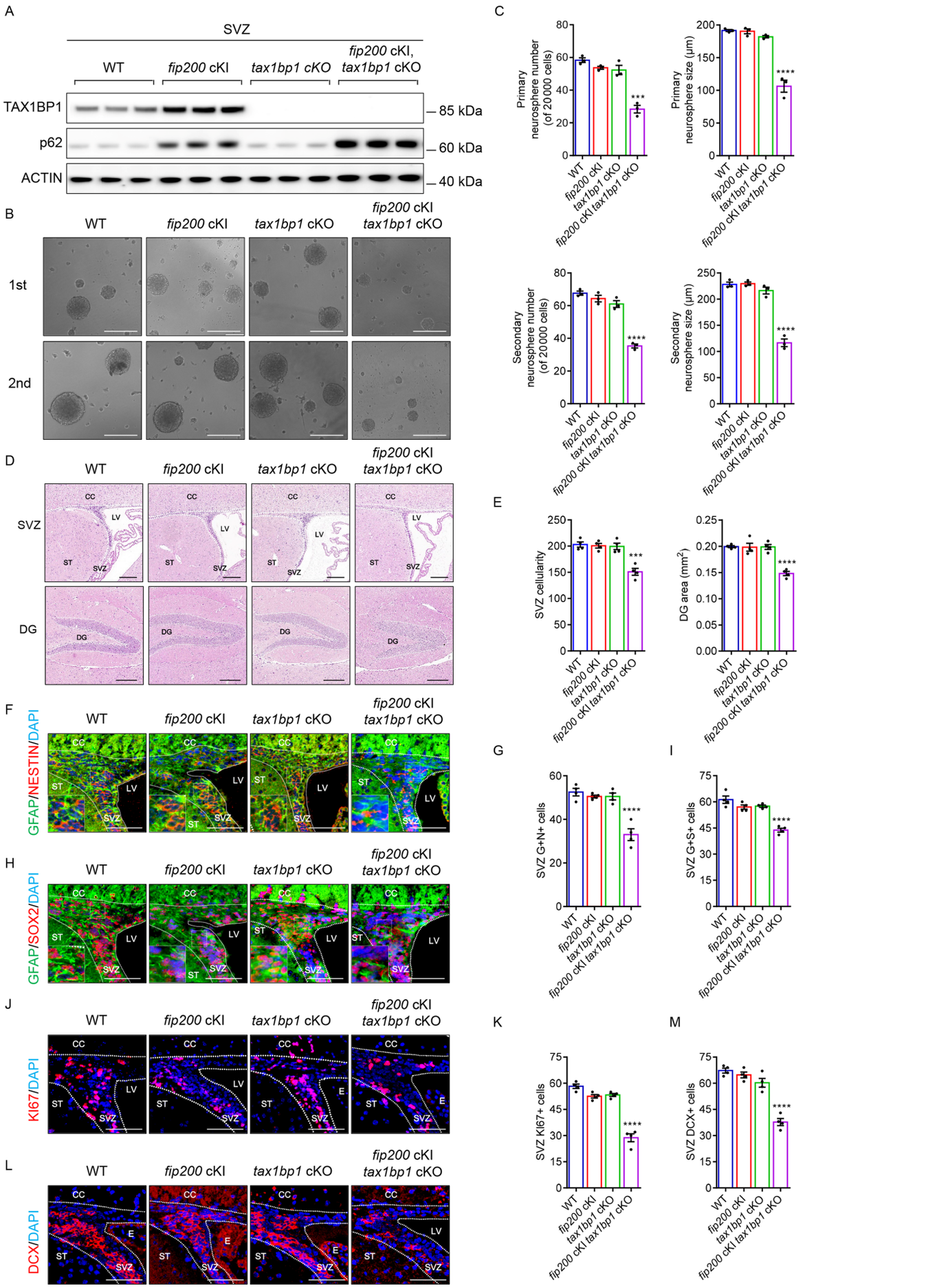
A
SVZ
WT
fip200 cKI
tax1bp1 cKO
fip200 cKI, tax1bp1 cKO
TAX1BP1
p62
ACTIN
85 kDa
60 kDa
40 kDa
B
1st
2nd
C
Primary neurosphere number (of 20000 cells)
Primary neurosphere size (μm)
Secondary neurosphere number (of 20000 cells)
Secondary neurosphere size (μm)
D
SVZ
DG
CC
LV
ST
E
F
GFAP/NESTIN/DAPI
G
SVZ G+N+ cells
H
GFAP/SOX2/DAPI
I
SVZ G+S+ cells
J
KI67/DAPI
K
SVZ KI67+ cells
L
DCX/DAPI
M
SVZ DCX+ cells
E
SVZ cellularity
DG area (mm²)

Figure 2 TAX1BP1 ablation in *fip200* cKI mice causes degeneration of SVZ due to NSC deficiency

A: Lysates were extracted from the SVZ of P28 WT, *fip200* cKI, *tax1bp1* cKO, and *fip200* cKI; *tax1bp1* cKO mice and analyzed by western blotting. ACTIN was used as a loading control. B: Primary (first) and secondary (second) neurosphere formation in WT, *fip200* cKI, *tax1bp1* cKO, and *fip200* cKI; *tax1bp1* cKO mice at P28. Representative phase contrast images. Scale bar: 200 μm. C: Mean±SEM of number and size of primary and secondary neurospheres (*n*=3 independent samples). ***: *P*<0.001; ****: *P*<0.0001 (one-way ANOVA with Dunnett's multiple comparisons test). D: Histological analysis of sagittal sections of SVZ and DG from WT, *fip200* cKI, *tax1bp1* cKO, and *fip200* cKI; *tax1bp1* cKO mice at P28. Dotted lines indicate boundaries of SVZ and DG. Scale bar: 200 μm. E: Mean±SEM of SVZ cellularity and DG area per section from WT (*n*=4), *fip200* cKI (*n*=4), *tax1bp1* cKO (*n*=4), and *fip200* cKI; *tax1bp1* cKO mice (*n*=4) at P28. ***: *P*<0.001; ****: *P*<0.0001 (one-way ANOVA with Dunnett's multiple comparisons test). F: Immunofluorescence of GFAP, NESTIN, and DAPI in SVZ from WT, *fip200* cKI, *tax1bp1* cKO, and *fip200* cKI; *tax1bp1* cKO mice at P28. Dotted lines indicate boundaries of SVZ. Scale bar: 50 μm. G: Mean±SEM of GFAP and NESTIN positive cells per SVZ section from WT (*n*=4), *fip200* cKI (*n*=4), *tax1bp1* cKO (*n*=4), and *fip200* cKI; *tax1bp1* cKO mice (*n*=4) at P28. ****: *P*<0.0001 (one-way ANOVA with Dunnett's multiple comparisons test). H: Immunofluorescence of GFAP, SOX2, and DAPI in SVZ from WT, *fip200* cKI, *tax1bp1* cKO, and *fip200* cKI; *tax1bp1* cKO mice at P28. Dotted lines indicate boundaries of SVZ. Scale bar: 50 μm. I: Mean±SEM of GFAP and SOX2 positive cells per SVZ section from WT (*n*=4), *fip200* cKI (*n*=4), *tax1bp1* cKO (*n*=4) and *fip200* cKI; *tax1bp1* cKO mice (*n*=4) at P28. ****: *P*<0.0001 (one-way ANOVA with Dunnett's multiple comparisons test). J: Immunofluorescence of KI67 and DAPI in SVZ from WT, *fip200* cKI, *tax1bp1* cKO, and *fip200* cKI; *tax1bp1* cKO mice at P28. Dotted lines indicate boundaries of SVZ. Scale bar: 50 μm. K: Mean±SEM of KI67 positive cells per SVZ section from WT (*n*=4), *fip200* cKI (*n*=4), *tax1bp1* cKO (*n*=4), and *fip200* cKI; *tax1bp1* cKO mice (*n*=4) at P28. ****: *P*<0.0001 (one-way ANOVA with Dunnett's multiple comparisons test). L: Immunofluorescence of DCX and DAPI in SVZ from WT, *fip200* cKI, *tax1bp1* cKO, and *fip200* cKI; *tax1bp1* cKO mice at P28. Dotted lines indicate boundaries of SVZ. Scale bar: 50 μm. M: Mean±SEM of DCX positive cells per SVZ section from WT (*n*=4), *fip200* cKI (*n*=4), *tax1bp1* cKO (*n*=4), and *fip200* cKI; *tax1bp1* cKO mice (*n*=4) at P28. ****: *P*<0.0001 (one-way ANOVA with Dunnett's multiple comparisons test).

correlating with NSC deficiency (Figure 2F–M; Supplementary Figure S2F–M). These findings were further validated *in vitro*, where elevated levels and aggregation of NBR1 and p62 were confirmed in *fip200* cKI; *tax1bp1* cKO neurospheres (Figure 3F–J; Supplementary Figure S3B). Collectively, these results indicate that the ablation of TAX1BP1 in *fip200* cKI mice leads to NSC deficiency primarily through the formation of p62/NBR1 aggregates, highlighting the essential role of TAX1BP1 in maintaining postnatal NSC health via aggrephagy.

FIP200-4A mutant elicits p62 aggregation via interactions with TAX1BP1 and NBR1

To identify the protein-protein interaction hierarchies required for p62 aggregate degradation via FIP200, we first evaluated the binding between recombinant epitope-tagged versions of FIP200-4A, NBR1, TAX1BP1, OPTN, and p62 proteins using immunoprecipitation-based assays. Interestingly, FIP200-4A co-immunoprecipitated with TAX1BP1 and NBR1 but not with p62 (Supplementary Figure S4A), implicating TAX1BP1 and NBR1 as potential enhancers of FIP200-p62 interactions. Consistent with this, our previous mass spectrometry analysis of mouse embryonic fibroblasts (MEFs) identified TAX1BP1 as the only aggrephagy receptor among the top 50 candidates regulating the FIP200-ATG13-ULK1 complex (Yang et al., 2022). Subsequent experiments revealed that NBR1 binds to TAX1BP1 along with forming self-interactions (Supplementary Figure S4B, C), while p62 interacts with itself, as well as NBR1, TAX1BP1, and OPTN to varying extents (Supplementary Figure S4D). Notably, associations between TAX1BP1 and NBR1 substantially enhanced the binding between FIP200 and p62 (Figure 4A). However, while NBR1 enhanced the binding between TAX1BP1 and p62, TAX1BP1 did not affect the NBR1-p62 association (Figure 4B; Supplementary Figure S4E). These findings establish the functional significance of TAX1BP1-NBR1 interactions, with TAX1BP1 directing the binding of FIP200-4A to p62 for subsequent degradation.

Next, we sought to identify the regions in TAX1BP1 essential for enabling p62 degradation via the FIP200-4A mutant. Using Flag-tagged TAX1BP1 truncation (Δ) constructs, reciprocal immunoprecipitation assays revealed that the NBR1 interaction region of TAX1BP1 existed within the 449–470 amino acid (aa) sequence (Supplementary Figure S4F), consistent with recent research identifying the interaction region between 420–506 aa (Ohnstad et al., 2020). To further refine the binding sites, we analyzed overlapping TAX1BP1Δ mutants lacking residues across the 449–470 aa sequence, which narrowed the binding region to between 449 and 463 aa (Supplementary Figure S4G). Alanine-scanning mutagenesis, where each set of four residues between 449 and 463 in TAX1BP1 was substituted with Ala (i.e., 449–452, 453–456, 457–460, and 461–464), was then employed to reconstruct interactions between TAX1BP1, NBR1, and p62 in HEK293T cells. Results revealed that only the 449–452 TAX1BP1 mutant (YREK to AAAA) failed to coprecipitate NBR1 and p62, while other alanine mutants showed enhanced TAX1BP1/p62 binding compared to intact TAX1BP1 (Figure 4C). Of note, the TAX1BP1$^{YREK449\text{-}452AAAA}$ mutant maintained its binding affinity for FIP200 and LC3B (Supplementary Figure S4H, I). These findings highlight YREK as an essential motif required for NBR1 binding, allowing the selective disruption of TAX1BP1-NBR1 interactions using a YREK mutant construct that preserves other relevant binding interactions.

TAX1BP1 mediates p62 aggrephagy by recruiting FIP200 and NBR1

To gain deeper mechanistic insights into how the non-canonical autophagy function of FIP200 maintains NSCs, we utilized the Flag-TAX1BP1$^{YREK449\text{-}452AAAA}$ mutant together with previously characterized TAX1BP1 constructs, including the V143S mutant, which disrupts binding to LC3 (Flag-TAX1BP1^{V143S}) (Sarraf et al., 2020) and the A114Q mutant, which disrupts TAX1BP1 binding to FIP200 (Flag-TAX1BP1^{A114Q}) (Ohnstad et al., 2020). WT TAX1BP1 (Flag-WT TAX1BP1) and these mutants were reintroduced into NSCs derived at P28 from *fip200* cKI; *tax1bp1* cKO mice. Notably, re-expression of Flag-WT TAX1BP1 and Flag-TAX1BP1^{V143S} but not Flag-TAX1BP1$^{YREK449\text{-}452AAAA}$ or Flag-TAX1BP1^{A114Q}, resulted in diminished p62 and NBR1 levels (Figure 4D; Supplementary Figure S4J). This pattern was also reflected in the levels of accumulated p62 aggregates within the cells (Figure 4E, F), indicating that the YREK449-

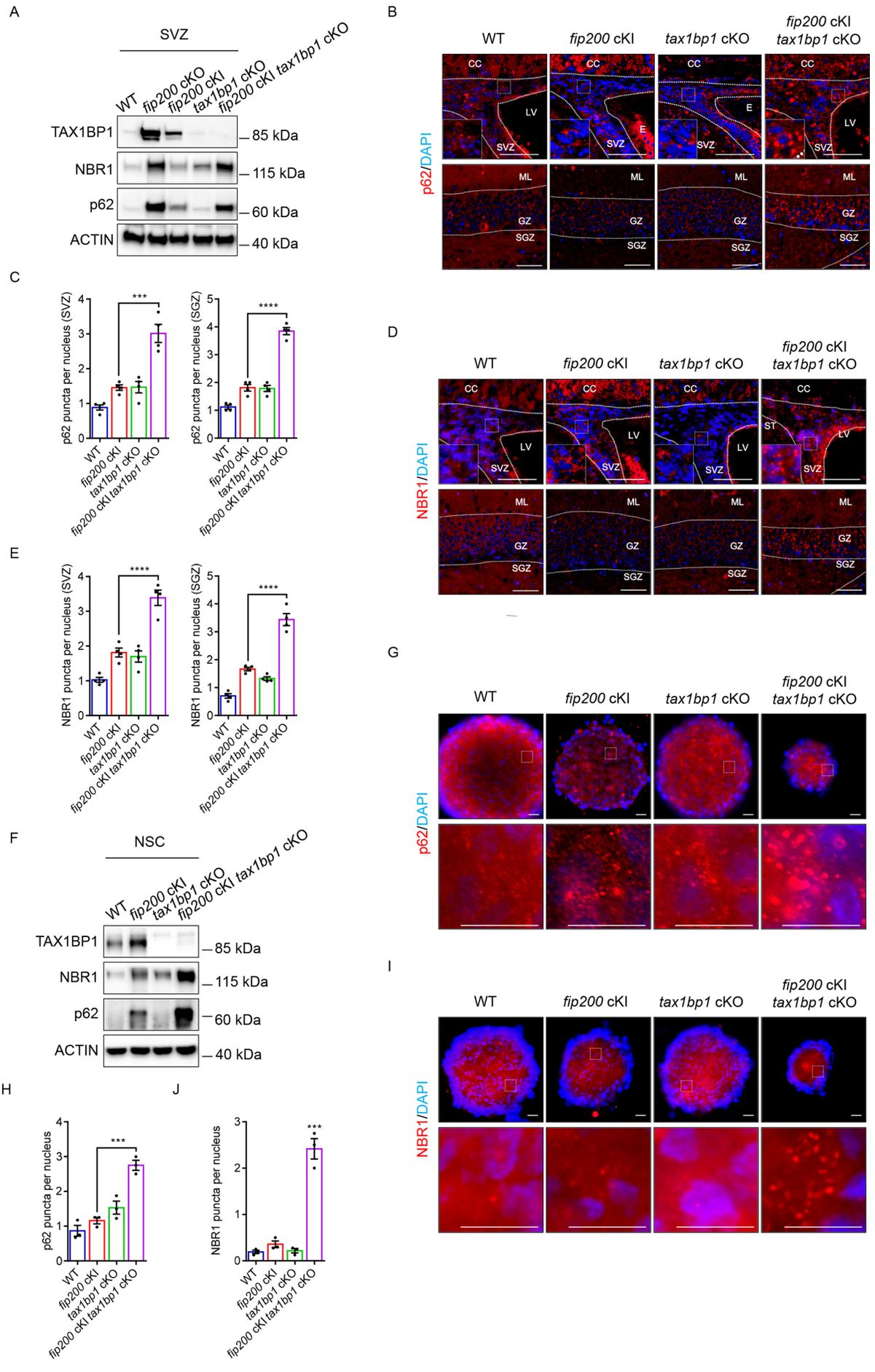
A
SVZ
WT
fip200 cKO
fip200 cKI
tax1bp1 cKO
fip200 cKI tax1bp1 cKO
TAX1BP1
NBR1
p62
ACTIN
85 kDa
115 kDa
60 kDa
40 kDa
B
WT
fip200 cKI
tax1bp1 cKO
fip200 cKI tax1bp1 cKO
p62/DAPI
CC
LV
SVZ
E
ST
ML
GZ
SGZ
C
p62 puncta per nucleus (SVZ)
p62 puncta per nucleus (SGZ)
***
****
D
NBR1/DAPI
E
NBR1 puncta per nucleus (SVZ)
NBR1 puncta per nucleus (SGZ)
F
NSC
G
I
H
J
p62 puncta per nucleus
NBR1 puncta per nucleus

Figure 3 TAX1BP1 ablation in *fip200* cKI mice causes p62 and NBR1 aggregation

A: Lysates were extracted from the SVZ of P28 WT, *fip200* cKI, *tax1bp1* cKO, and *fip200* cKI; *tax1bp1* cKO mice, with TAX1BP1, NBR1, and p62 protein levels analyzed by western blotting. ACTIN was used as a loading control. B: Immunofluorescence of p62 puncta and DAPI in SVZ and SGZ from WT, *fip200* cKI, *tax1bp1* cKO, and *fip200* cKI; *tax1bp1* cKO mice at P28. Dotted lines indicate boundaries of SVZ and DG. Scale bar: 50 μm. C: Mean±SEM of p62 puncta per SVZ and SGZ section from WT (*n*=4), *fip200* cKI (*n*=4), *tax1bp1* cKO (*n*=4), and *fip200* cKI; *tax1bp1* cKO mice (*n*=4) at P28. ***: *P*<0.001; ****: *P*<0.0001 (one-way ANOVA with Dunnett's multiple comparisons test). D: Immunofluorescence of NBR1 puncta and DAPI in SVZ and SGZ from WT, *fip200* cKI, *tax1bp1* cKO, and *fip200* cKI; *tax1bp1* cKO mice at P28. Dotted lines indicate boundaries of SVZ and DG. Scale bar: 50 μm. E: Mean±SEM of NBR1 puncta per SVZ and SGZ section from WT (*n*=4), *fip200* cKI (*n*=4), *tax1bp1* cKO (*n*=4), and *fip200* cKI; *tax1bp1* cKO mice (*n*=4) at P28. ****: *P*<0.0001 (one-way ANOVA with Dunnett's multiple comparisons test). F: Lysates were extracted from NSC of P28 WT, *fip200* cKI, *tax1bp1* cKO, and *fip200* cKI; *tax1bp1* cKO mice, with TAX1BP1, NBR1, and p62 protein levels analyzed by western blotting. ACTIN was used as a loading control. G: Immunofluorescence of p62 puncta and DAPI in neurospheres from WT, *fip200* cKI, *tax1bp1* cKO, and *fip200* cKI; *tax1bp1* cKO mice at P28. Scale bar: 20 μm. H: Mean±SEM of p62 puncta per neurosphere (*n*=3 independent samples). ***: *P*<0.001 (one-way ANOVA with Dunnett's multiple comparisons test). I: Immunofluorescence of NBR1 puncta and DAPI in neurospheres from WT, *fip200* cKI, *tax1bp1* cKO, and *fip200* cKI; *tax1bp1* cKO mice at P28. Scale bar: 20 μm. J: Mean±SEM of NBR1 puncta per neurosphere (*n*=3 independent samples). ***: *P*<0.001 (one-way ANOVA with Dunnett's multiple comparisons test).

452AAAA and A114Q mutants fail to degrade p62 aggregates. Furthermore, neurosphere assays confirmed that the reintroduction of WT and V143S TAX1BP1 constructs increased the size and number of neurospheres, while the YREK449-452AAAA and A114Q mutants did not significantly affect NSC potency (Figure 4G, H). These findings suggest that TAX1BP1 is required for p62 aggrephagy through FIP200, with relevance for its degradation in NSCs.

TAX1BP1 ablation in *fip200* cKO mice exacerbates p62/NBR1 aggregation and degeneration of SVZ and DG

Given that TAX1BP1 ablation increased p62/NBR1 aggregation and NSC deficiency in *fip200* cKI mice, we next sought to demonstrate the function of TAX1BP1 in *fip200* cKO mice. We first explored how manipulating TAX1BP1 affected NBR1 and p62 protein levels in SVZ tissues across different experimental backgrounds. Interestingly, a marked up-regulation in NBR1 and p62 was observed in the SVZ of *fip200* cKO; *tax1bp1* cKO mice (designated *2* cKO) compared to *fip200* cKO and *fip200* cKI; *tax1bp1* cKO mice (Figure 5A; Supplementary Figure S5A). NBR1 and p62 aggregates were also significantly increased in the SVZ and DG regions of *2* cKO mice (Figure 5B–E), aligning with the observations of NSC deficiency (Figure 5F–O; Supplementary Figure S5B–G). Previous studies have indicated that primary neurospheres generated from P0 *fip200* cKO mice are similar in size and number to those from WT mice (Wang et al., 2013). However, the neurosphere assays showed marked reductions in neurosphere formation in both primary and secondary SVZ cultures derived from P0 *2* cKO mice (Figure 5P, Q). For neurospheres isolated from P28 mice, no differences in sphere size or number were observed between *fip200* cKO and *2* cKO mice. Collectively, these results indicate that the degradation of p62 aggregates in NSCs via aggrephagy proceeds efficiently only when TAX1BP1 and FIP200 are co-expressed.

DISCUSSION

The core canonical autophagy proteins form the ULK1-ATG13-FIP200-ATG101 and PI3K-BECLIN1-ATG14L1-VPS34 complexes, which are required for the induction and initiation of autophagosomes, while two ubiquitin-like conjugation systems, ATG7-ATG12-ATG5-ATG16L1 and ATG8, are involved in the elongation of autophagosomes (Galluzzi et al., 2017; He & Klionsky, 2009; Mizushima & Levine, 2010).

Previous research has shown that cells can degrade substrates via *Atg7*-independent and autophagy receptor-dependent mechanisms, namely non-canonical autophagy (Ohnstad et al., 2020). Interestingly, unlike *Fip200*, the ablation of core autophagosome elongation genes such as *Atg5*, *Atg7*, and *Atg16L1* does not significantly impair p62 aggregate degradation or NSC functionality. In *fip200*^{hGFAP} cKO mice, the accumulation of p62 aggregates triggers aberrant increases in superoxide by impairing superoxide dismutase functions, which affects the fate of autophagy-deficient NSCs (Wang et al., 2016). In addition, p62 aggregates can hinder NSC differentiation by promoting increased infiltration and activation of microglia through a p53-independent, non-cell autonomous mechanism (Wang et al., 2017). This difference highlights the essential role of the non-canonical function of FIP200 in NSC maintenance and differentiation.

Aggrephagy is a specialized cellular mechanism designed to degrade protein aggregates, relying on specific cargo receptors (Lamark & Johansen, 2012). Six aggrephagy receptors —TAX1BP1, NBR1, P62, OPTN, TOLLIP, and CCT2—have been identified and implicated in the degradation of ubiquitinated protein aggregates (Gibertini et al., 2023; Ma et al., 2022; Sarraf et al., 2020; Trapannone et al., 2023). In this study, we found that among these six receptors, only TAX1BP1, NBR1, and p62 aggregates significantly accumulated in NSCs that were impaired by the absence of FIP200. Interestingly, individual knockdown of TAX1BP1, NBR1, and p62 in WT, *fip200* cKO, *fip200* cKI NSCs produced different phenotypes, with only TAX1BP1 knockdown leading to significant increases in p62 and NBR1 protein levels in *fip200* cKI NSCs. Moreover, knockdown of TAX1BP1 further impaired the self-renewal capacity of *fip200* cKO and *fip200* cKI NSCs, while knockdown of p62 largely reversed these defects. These insights suggest that autophagy receptors play different roles in NSC self-renewal, particularly under the context of canonical autophagy deficiency.

To investigate the non-canonical functions of FIP200 and its partner TAX1BP1, *fip200* cKO, *fip200* cKI, *tax1bp1* cKO, *fip200* cKI; *tax1bp1* cKO, and *fip200*; *tax1bp1 2* cKO mice were generated. The *fip200* cKI mice were designed to express a FIP200-4A mutant incapable of binding with ATG13, thus disrupting the formation of the canonical autophagy induction complex. This model allowed us to study the non-canonical interactions involving FIP200 and other proteins (Chen et al., 2016). By leveraging the differential outcomes observed in these mouse models, we demonstrated that the degradation of p62 aggregates primarily occurred via FIP200-

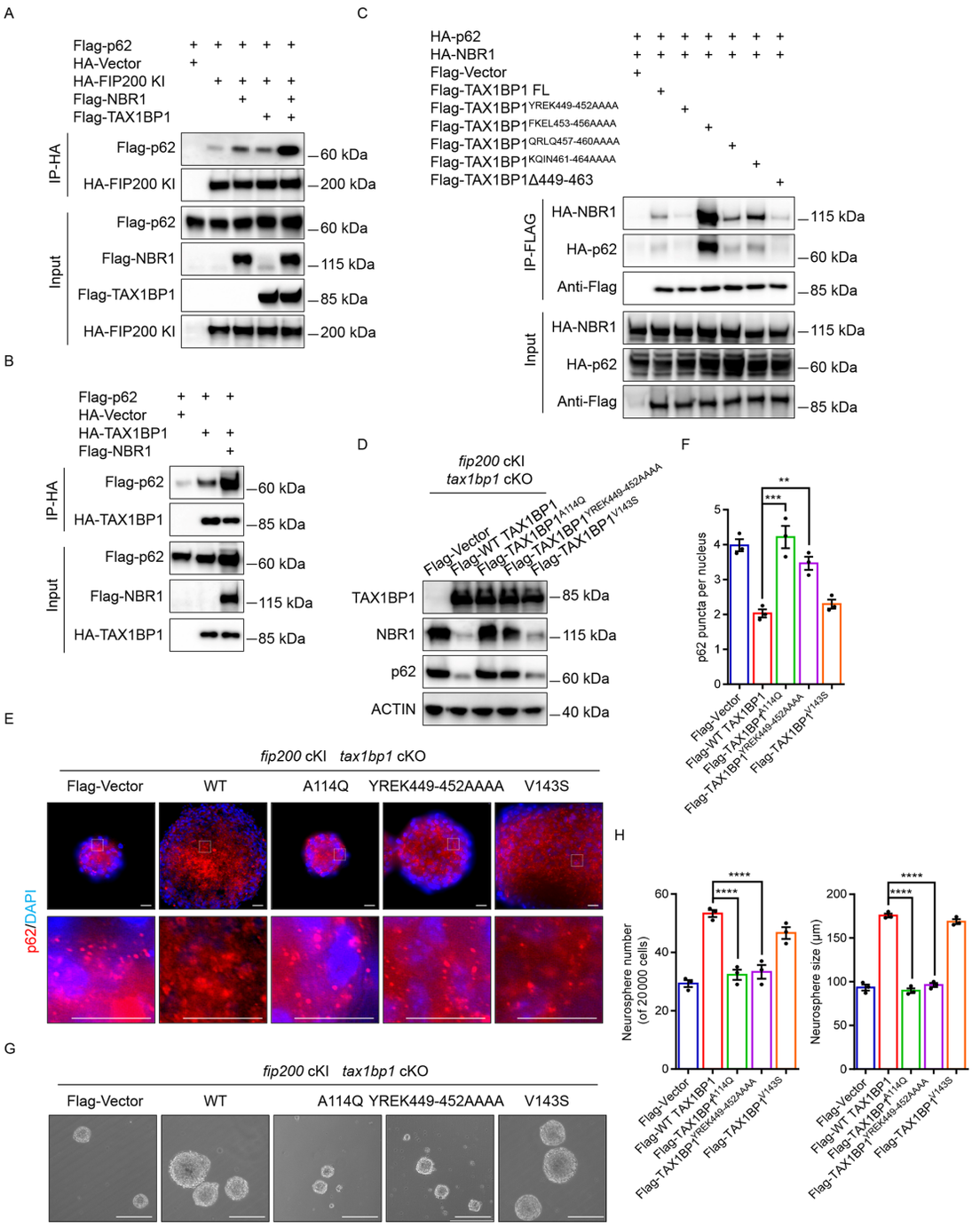

Figure 4 TAX1BP1 mediates p62 aggregate aggrephagy by recruiting FIP200 and NBR1

A: Co-immunoprecipitation assays in HEK293T cells after co-transfection with Flag-p62 and indicated combinations of empty HA-vector and HA-tagged FIP200 KI with or without Flag-TAX1BP1 or Flag-NBR1 before immunoprecipitation with anti-HA magnetic agarose. Immunoprecipitates (top panel) and input samples (bottom panel) were then subjected to western blotting against anti-Flag or HA. B: Co-immunoprecipitation assays in HEK293T cells after co-transfection with Flag-p62 and indicated combinations of empty HA-vector and HA-tagged TAX1BP1 with or without Flag-NBR1 before immunoprecipitation with anti-HA magnetic agarose. Immunoprecipitates (top panel) and input samples (bottom panel) were then subjected to western blotting against anti-Flag or HA. C: Co-immunoprecipitation assays in HEK293T cells after co-transfection with HA-p62, HA-NBR1, and indicated combinations of empty Flag-vector, Flag-tagged TAX1BP1 FL, YREK449-452AAAA, FKEL453-456AAAA, QRLQ457-460AAAA, KQIN461-464AAAA, and Δ449-463 before immunoprecipitation with anti-DYKDDDDK magnetic agarose. Immunoprecipitates (top panel) and input samples (bottom panel) were then subjected to western blotting against anti-HA or Flag. D: Western blotting of TAX1BP1, NBR1, and p62 protein levels in *fip200* cKI; *tax1bp1* cKO NSCs re-expressed with different TAX1BP1 mutants. ACTIN was used as a loading control. E: Immunofluorescence of p62 puncta and DAPI in *fip200* cKI; *tax1bp1* cKO NSCs re-expressed with different TAX1BP1 mutants. Scale bar: 20 μm. F: Mean±SEM of p62 puncta per neurosphere (n=3 independent samples). **: P<0.01; ***: P<0.001 (one-way ANOVA with Dunnett's multiple comparisons test). G: Neurosphere formation from *fip200* cKI; *tax1bp1* cKO NSCs re-expressed with different TAX1BP1 mutants. Representative phase contrast images. Scale bar: 200 μm. H: Mean±SEM of number and size of neurospheres (n=3 independent samples). ****: P<0.0001 (one-way ANOVA with Dunnett's multiple comparisons test).

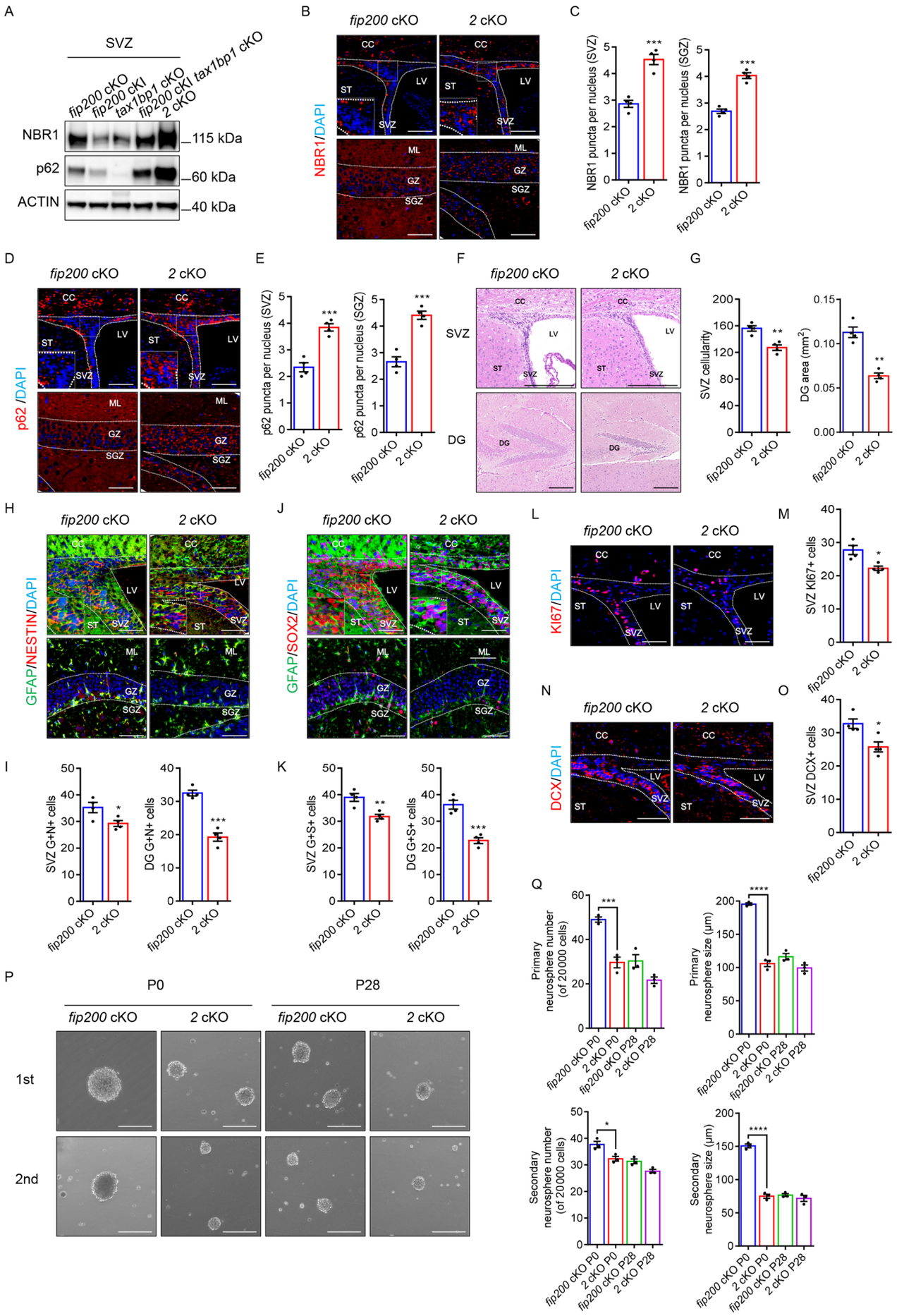
A
SVZ
fip200 cKO
fip200 cKI
tax1bp1 cKO
fip200 cKI tax1bp1 cKO
2 cKO
NBR1
p62
ACTIN
115 kDa
60 kDa
40 kDa
B
fip200 cKO
2 cKO
NBR1/DAPI
CC
ST
LV
SVZ
ML
GZ
SGZ
C
NBR1 puncta per nucleus (SVZ)
NBR1 puncta per nucleus (SGZ)
***
fip200 cKO
2 cKO
D
fip200 cKO
2 cKO
p62 /DAPI
E
p62 puncta per nucleus (SVZ)
p62 puncta per nucleus (SGZ)
F
fip200 cKO
2 cKO
SVZ
DG
G
SVZ cellularity
DG area (mm²)
**
H
fip200 cKO
2 cKO
GFAP/NESTIN/DAPI
I
SVZ G+N+ cells
DG G+N+ cells
*
J
fip200 cKO
2 cKO
GFAP/SOX2/DAPI
K
SVZ G+S+ cells
DG G+S+ cells
L
fip200 cKO
2 cKO
KI67/DAPI
M
SVZ KI67+ cells
N
fip200 cKO
2 cKO
DCX/DAPI
O
SVZ DCX+ cells
P
P0
P28
fip200 cKO
2 cKO
1st
2nd
Q
Primary neurosphere number (of 20000 cells)
Primary neurosphere size (μm)
Secondary neurosphere number (of 20000 cells)
Secondary neurosphere size (μm)
fip200 cKO P0
2 cKO P0
fip200 cKO P28
2 cKO P28

Figure 5 TAX1BP1 ablation in *fip200* cKO mice exacerbates p62/NBR1 aggregation and degeneration of the SVZ and DG

A: Lysates were extracted from the SVZ of P28 *fip200* cKO, *fip200* cKI, *tax1bp1* cKO, *fip200* cKI; *tax1bp1* cKO, and *2* cKO mice, with NBR1 and p62 protein levels analyzed by western blotting. ACTIN was used as a loading control. B: Immunofluorescence of NBR1 puncta and DAPI in SVZ and SGZ from *fip200* cKO and *2* cKO mice at P28. Dotted lines indicate boundaries of SVZ and DG. Scale bar: 100 μm. C: Mean±SEM of NBR1 puncta per SVZ and SGZ section from *fip200* cKO (*n*=4) and *2* cKO mice (*n*=4) at P28. ***: *P*<0.001 (unpaired Student's two-tailed *t*-test). D: Immunofluorescence of p62 puncta and DAPI in SVZ and SGZ from *fip200* cKO and *2* cKO mice at P28. Dotted lines indicate boundaries of SVZ and DG. Scale bar: 100 μm. E: Mean±SEM of p62 puncta per SVZ and SGZ section from *fip200* cKO (*n*=4) and *2* cKO mice (*n*=4) at P28. ***: *P*<0.001 (unpaired Student's two-tailed *t*-test). F: Histological analysis of sagittal sections of SVZ and DG from *fip200* cKO and *2* cKO mice at P28. Dotted lines indicate boundaries of SVZ and DG. Scale bar: 200 μm. G: Mean±SEM of SVZ cellularity and DG area per section from *fip200* cKO (*n*=4) and *2* cKO mice (*n*=4) at P28. **: *P*<0.01 (unpaired Student's two-tailed *t*-test). H: Immunofluorescence of GFAP, NESTIN, and DAPI in SVZ and SGZ from *fip200* cKO and *2* cKO mice at P28. Dotted lines indicate boundaries of SVZ and DG. Scale bar: 50 μm. I: Mean±SEM of GFAP and NESTIN positive cells per SVZ and SGZ section from *fip200* cKO (*n*=4) and *2* cKO mice (*n*=4) at P28. *: *P*<0.05; ***: *P*<0.001 (unpaired Student's two-tailed *t*-test). J: Immunofluorescence of GFAP, SOX2, and DAPI in SVZ and SGZ from *fip200* cKO and *2* cKO mice at P28. Dotted lines indicate boundaries of SVZ and DG. Scale bar: 50 μm. K: Mean±SEM of GFAP and SOX2 positive cells per SVZ and SGZ section from *fip200* cKO (*n*=4) and *2* cKO mice (*n*=4) at P28. **: *P*<0.01; ***: *P*<0.001 (unpaired Student's two-tailed *t*-test). L: Immunofluorescence of KI67 and DAPI in SVZ from *fip200* cKO and *2* cKO mice at P28. Dotted lines indicate boundaries of SVZ. Scale bar: 50 μm. M: Mean±SEM of KI67 positive cells per SVZ section from *fip200* cKO (*n*=4) and *2* cKO mice (*n*=4) at P28. *: *P*<0.05 (unpaired Student's two-tailed t-test). N: Immunofluorescence of DCX and DAPI in SVZ from *fip200* cKO and *2* cKO mice at P28. Dotted lines indicate boundaries of SVZ. Scale bar: 50 μm. O: Mean±SEM of DCX positive cells per SVZ section from *fip200* cKO (*n*=4) and *2* cKO mice (*n*=4) at P28. *: *P*<0.05 (unpaired Student's two-tailed t-test). P: Primary (first) and secondary (second) neurosphere formation from *fip200* cKO and *2* cKO mice at P0 and P28. Representative phase contrast images. Scale bar: 200 μm. Q: Mean±SEM of number and size of primary and secondary neurospheres (*n*=3 independent samples). *: *P*<0.05; ***: *P*<0.001; ****: *P*<0.0001 (one-way ANOVA with Dunnett's multiple comparisons test).

TAX1BP1-NBR1 axis-mediated non-canonical autophagy. Furthermore, the abnormal accumulation of p62 aggregates impaired NSC maintenance and differentiation. These insights fundamentally extend our understanding of autophagy in NSCs and present potential therapeutic avenues for addressing NSC maintenance and neurodegenerative conditions linked to protein aggregation.

A key innovation of our study was the use of the FIP200-4A mutant, which successfully rescued all observed phenotypes in *fip200* cKO mice, highlighting its critical role in the degradation of ubiquitinated protein aggregates. To further validate this role, we developed a model with both FIP200-4A and TAX1BP1 KO (*fip200* cKI; *tax1bp1* cKO mice), which mimicked the phenotypes observed in *fip200* cKO mice, thereby implicating TAX1BP1 as a necessary component in FIP200-4A-mediated degradation. Moreover, the *fip200* cKI; *tax1bp1* cKO mice mirrored the phenotypes of *fip200* cKO mice, suggesting that TAX1BP1 is necessary for FIP200-4A mutant-mediated degradation. The *fip200*; *tax1bp1 2* cKO mice also showed more severe phenotypes than those observed in *fip200* cKO mice at P28, indicating that TAX1BP1 also contributes to aggrephagy independently of FIP200-mediated degradation, as illustrated in our working model (Figure 6). In addition, $fip200^{hGFAP}$ cKO; $p62^{-/-}$ mice showed rescued phenotypes similar to those observed in $fip200^{hGFAP}$ cKO mice at P28, consistent with previous study (Wang et al., 2016), indicating that p62 aggregation is a major mediator for FIP200 mutant NSCs.

Beyond its central role in the autophagy initiation complex, FIP200 interacts with various proteins to direct alternative cellular functions (Yeo et al., 2020). Structural and biochemical studies have revealed that FIP200 directly interacts with p62 through its claw region to facilitate the degradation of p62-ubiquitinated protein aggregates (Turco et al., 2019a, 2019b). The FIP200 claw region is also responsible for interactions with OPTN or CCPG1 (Zhou et al., 2021). Additionally, FIP200 associates with NDP52 via its coiled-coil region, promoting NDP52-mediated xenophagy (Boyle et al., 2019; Shi et al., 2020) and mitophagy (Yamano & Youle, 2020). In *Fip200* KO cells, TBK1 is recruited to p62 aggregates via TAX1BP1, promoting p62 aggregate formation (Liu et al., 2021; Schlütermann et al., 2021), whereas, in *Atg7* KO cells, TAX1BP1 recruits FIP200 to bind to NBR1, resulting in local autophagosome formation (Ohnstad et al., 2020). Recent *in vitro* reconstitution research identified direct interactions between FIP200, TAX1BP1, NBR1, and p62, with p62 and NBR1 highlighted as major drivers of ubiquitin condensate formation, whereby NBR1 recruits TAX1BP1 to the ubiquitin condensates formed by p62. Although all three receptors interact with FIP200, TAX1BP1 is the main driver of FIP200 recruitment, thereby mediating the autophagic degradation of p62-ubiquitin condensates (Turco et al., 2021). These *in vitro* observations complement the findings in this study. To the best of our knowledge, however, this study is the first to elucidate the mechanistic basis for the degradation of p62 aggregates in NSCs via non-canonical autophagy.

Our data showed that the interactions between FIP200, TAX1BP1, NBR1, and p62 are crucial for the degradation of p62 aggregates in NSCs. We found that FIP200 preferentially binds with TAX1BP1 and NBR1, both of which enhance the interaction between FIP200 and p62. Additionally, TAX1BP1 showed a tendency to bind with NBR1, facilitating the interaction between TAX1BP1 and p62. Disrupting any of these interactions impaired degradation of p62 aggregates. Further targeted experiments revealed that similar to the phenotype observed in *fip200* cKO mice, TAX1BP1 ablation in *fip200* cKI mice caused p62 and NBR1 aggregation and degeneration of the SVZ and DG. These findings underscore the role of TAX1BP1 as a key driver of p62 aggregate degradation in canonical autophagy-defective NSCs.

In summary, our study revealed a non-canonical autophagy pathway involved in protein aggregate degradation and the regulation of postnatal NSCs. We identified TAX1BP1 as a key determinant of p62 aggregate degradation and NSC regulation in *fip200* cKI mice. Further research is required to fully elucidate the clinical relevance of this pathway in neurodegenerative diseases.

SUPPLEMENTARY DATA

Supplementary data to this article can be found online.

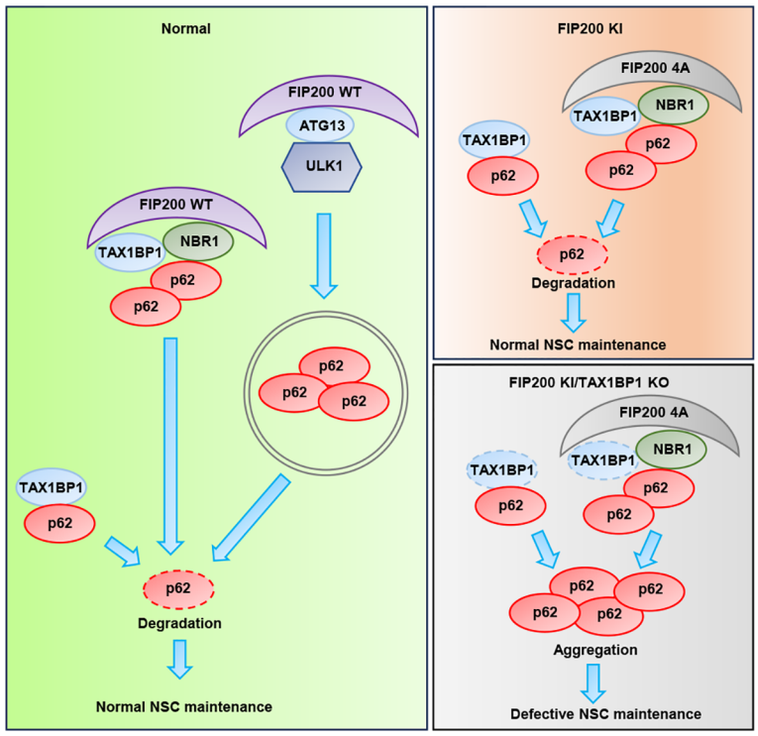

Figure 6 Working model of FIP200-TAX1BP1 axis-mediated non-canonical autophagy of p62 aggregates, leading to normal neural stem cell (NSC) maintenance

Schematic of differential p62 aggregate degradation in NSCs. Macroautophagy, FIP200-TAX1BP1 axis-mediated non-canonical autophagy, and TAX1BP1-mediated non-canonical autophagy mediate the degradation of p62 aggregates, leading to normal NSC maintenance.

COMPETING INTERESTS

The authors declare that they have no competing interests.

AUTHORS' CONTRIBUTIONS

S.C. and M.W. conceived and designed the project; S.C. and M.W. supervised the study; Y.F.Z. and R.H.Y. performed most of the experiments; S.Z., P.P.T., R.Z., Y.X.W., J.L.Z., Y.Y.W., J.M.W., M.K.L., and X.J.S. assisted with most of the cloning and mouse experiments; X.D.Z., Y.W.Z., and G.Z.L. provided reagents and resources; R.X., R.F.T, X.D.Z., S.C., and M.W. carried out data analysis. Y.F.Z., R.F.T., and S.C. wrote the manuscript. All authors read and approved the final version of the manuscript.

ACKNOWLEDGMENTS

We would like to thank Dr. Jun-Lin Guan from the University of Cincinnati for providing *fip200* flox/KI mice. We thank Dr. Wei-Lin Jin from Lanzhou University for helpful discussions. We thank all the staff of the Laboratory Animal Center of Zhengzhou University for maintaining the animals.

REFERENCES

Becher OJ, Holland EC. 2010. Evidence for and against regional differences in neural stem and progenitor cells of the CNS. *Genes & Development*, **24**(20): 2233–2238.

Bhutia SK, Praharaj PP, Bhol CS, et al. 2018. Monitoring and measuring mammalian autophagy. *In*: Turksen K. Autophagy in Differentiation and Tissue Maintenance. New York: Humana Press, 209–222.

Bjørkøy G, Lamark T, Johansen T. 2006. p62/SQSTM1: a missing link between protein aggregates and the autophagy machinery. *Autophagy*, **2**(2): 138–139.

Boyle KB, Ravenhill BJ, Randow F. 2019. CALCOCO2/NDP52 initiates selective autophagy through recruitment of ULK and TBK1 kinase complexes. *Autophagy*, **15**(9): 1655–1656.

Casares-Crespo L, Calatayud-Baselga I, García-Corzo L, et al. 2018. On the role of basal autophagy in adult neural stem cells and neurogenesis. *Frontiers in Cellular Neuroscience*, **12**: 339.

Chen S, Wang CR, Yeo S, et al. 2016. Distinct roles of autophagy-dependent and -independent functions of FIP200 revealed by generation and analysis of a mutant knock-in mouse model. *Genes & Development*, **30**(7): 856–869.

Deng ZQ, Lim J, Wang Q, et al. 2020. ALS-FTLD-linked mutations of SQSTM1/p62 disrupt selective autophagy and NFE2L2/NRF2 anti-oxidative stress pathway. *Autophagy*, **16**(5): 917–931.

Doetsch F, Caillé I, Lim DA, et al. 1999. Subventricular zone astrocytes are neural stem cells in the adult mammalian brain. *Cell*, **97**(6): 703–716.

Donde A, Sun MK, Jeong YH, et al. 2020. Upregulation of ATG7 attenuates motor neuron dysfunction associated with depletion of TARDBP/TDP-43. *Autophagy*, **16**(4): 672–682.

Fleming A, Rubinsztein DC. 2020. Autophagy in neuronal development and plasticity. *Trends in Neurosciences*, **43**(10): 767–779.

Friesen EL, Zhang YT, Earnshaw R, et al. 2020. BAG5 promotes alpha-synuclein oligomer formation and functionally interacts with the autophagy adaptor protein p62. *Frontiers in Cell and Developmental Biology*, **8**: 716.

Gage FH. 2000. Mammalian neural stem cells. *Science*, **287**(5457): 1433–1438.

Galluzzi L, Baehrecke EH, Ballabio A, et al. 2017. Molecular definitions of autophagy and related processes. *The EMBO Journal*, **36**(13): 1811–1836.

Gibertini S, Ruggieri A, Cheli M, et al. 2023. Protein aggregates and aggrephagy in myopathies. *International Journal of Molecular Sciences*, **24**(9): 8456.

Guo CT, Zhao Y. 2020. Autophagy and DNA damage repair. *Genome Instability & Disease*, **1**(4): 172–183.

He CC, Klionsky DJ. 2009. Regulation mechanisms and signaling pathways of autophagy. *Annual Review of Genetics*, **43**: 67–93.

Huang J, Klionsky DJ. 2007. Autophagy and human disease. *Cell Cycle*, **6**(15): 1837–1849.

Klionsky DJ, Petroni G, Amaravadi RK, et al. 2021. Autophagy in major human diseases. *The EMBO Journal*, **40**(19): e108863.

Lamark T, Johansen T. 2012. Aggrephagy: selective disposal of protein aggregates by macroautophagy. *International Journal of Cell Biology*, **2012**: 736905.

Liang CC, Wang CR, Peng X, et al. 2010. Neural-specific deletion of FIP200 leads to cerebellar degeneration caused by increased neuronal death and axon degeneration. *Journal of Biological Chemistry*, **285**(5): 3499–3509.

Liu H, Wang CR, Yi F, et al. 2021. Non-canonical function of FIP200 is required for neural stem cell maintenance and differentiation by limiting TBK1 activation and p62 aggregate formation. *Scientific Reports*, **11**(1): 23907.

Liu YH, Lai WS, Tsay HJ, et al. 2013. Effects of maternal immune activation on adult neurogenesis in the subventricular zone-olfactory bulb pathway and olfactory discrimination. *Schizophrenia Research*, **151**(1-3): 1–11.

Lyu L, Chen Z, McCarty N. 2022. TRIM44 links the UPS to SQSTM1/p62-dependent aggrephagy and removing misfolded proteins. *Autophagy*, **18**(4): 783–798.

Ma SF, Attarwala IY, Xie XQ. 2019. SQSTM1/p62: a potential target for neurodegenerative disease. *ACS Chemical Neuroscience*, **10**(5): 2094–2114.

Ma XY, Lu CJ, Chen YT, et al. 2022. CCT2 is an aggrephagy receptor for clearance of solid protein aggregates. *Cell*, **185**(8): 1325–1345. e22.

Majcher V, Goode A, James V, et al. 2015. Autophagy receptor defects and ALS-FTLD. *Molecular and Cellular Neuroscience*, **66**: 43–52.

Mizushima N, Levine B. 2010. Autophagy in mammalian development and differentiation. *Nature Cell Biology*, **12**(9): 823–830.

Oh CK, Dolatabadi N, Cieplak P, et al. 2022. S-nitrosylation of p62 inhibits autophagic flux to promote α-synuclein secretion and spread in parkinson's disease and lewy body dementia. *Journal of Neuroscience*, **42**(14): 3011–3024.

Ohnstad AE, Delgado JM, North BJ, et al. 2020. Receptor-mediated clustering of FIP200 bypasses the role of LC3 lipidation in autophagy. *The EMBO Journal*, **39**(24): e104948.

Palmer TD, Takahashi J, Gage FH. 1997. The adult rat hippocampus contains primordial neural stem cells. *Molecular and Cellular Neuroscience*, **8**(6): 389–404.

Pankiv S, Clausen TH, Lamark T, et al. 2007. p62/SQSTM1 binds directly to Atg8/LC3 to facilitate degradation of ubiquitinated protein aggregates by autophagy. *Journal of Biological Chemistry*, **282**(33): 24131–24145.

Rué L, López-Soop G, Gelpi E, et al. 2013. Brain region- and age-dependent dysregulation of p62 and NBR1 in a mouse model of Huntington's disease. *Neurobiology of Disease*, **52**: 219–228.

Sarraf SA, Shah HV, Kanfer G, et al. 2020. Loss of TAX1BP1-directed autophagy results in protein aggregate accumulation in the brain. *Molecular Cell*, **80**(5): 779–795. e10.

Schaeffer V, Goedert M. 2012. Stimulation of autophagy is neuroprotective in a mouse model of human tauopathy. *Autophagy*, **8**(11): 1686–1687.

Schlütermann D, Berleth N, Deitersen J, et al. 2021. FIP200 controls the TBK1 activation threshold at SQSTM1/p62-positive condensates. *Scientific Reports*, **11**(1): 13863.

Shi XS, Chang CM, Yokom AL, et al. 2020. The autophagy adaptor NDP52 and the FIP200 coiled-coil allosterically activate ULK1 complex membrane recruitment. *eLife*, **9**: e59099.

Thorburn A. 2018. Autophagy and disease. *Journal of Biological Chemistry*, **293**(15): 5425–5430.

Trapannone R, Romanov J, Martens S. 2023. p62 and NBR1 functions are dispensable for aggrephagy in mouse ESCs and ESC-derived neurons. *Life Science Alliance*, **6**(11): e202301936.

Turco E, Savova A, Gere F, et al. 2021. Reconstitution defines the roles of p62, NBR1 and TAX1BP1 in ubiquitin condensate formation and autophagy initiation. *Nature Communications*, **12**(1): 5212.

Turco E, Witt M, Abert C, et al. 2019a. FIP200 claw domain binding to p62 promotes autophagosome formation at ubiquitin condensates. *Molecular Cell*, **74**(2): 330–346. e11.

Turco E, Witt M, Abert C, et al. 2019b. How RB1CC1/FIP200 claws its way to autophagic engulfment of SQSTM1/p62-ubiquitin condensates. *Autophagy*, **15**(8): 1475–1477.

Vázquez P, Arroba AI, Cecconi F, et al. 2012. Atg5 and Ambra1 differentially modulate neurogenesis in neural stem cells. *Autophagy*, **8**(2): 187–199.

Wang CR, Chen S, Yeo S, et al. 2016. Elevated p62/SQSTM1 determines the fate of autophagy-deficient neural stem cells by increasing superoxide. *Journal of Cell Biology*, **212**(5): 545–560.

Wang CR, Liang CC, Bian ZC, et al. 2013. FIP200 is required for maintenance and differentiation of postnatal neural stem cells. *Nature Neuroscience*, **16**(5): 532–542.

Wang CR, Yeo S, Haas MA, et al. 2017. Autophagy gene FIP200 in neural progenitors non-cell autonomously controls differentiation by regulating microglia. *Journal of Cell Biology*, **216**(8): 2581–2596.

Wang SK, Li BG, Qiao HM, et al. 2014. Autophagy-related gene Atg5 is essential for astrocyte differentiation in the developing mouse cortex. *EMBO Reports*, **15**(10): 1053–1061.

Wang Y, Yang J, Zheng HR, et al. 2009. Expression of mutant p53 proteins implicates a lineage relationship between neural stem cells and malignant astrocytic glioma in a murine model. *Cancer Cell*, **15**(6): 514–526.

Xi Y, Dhaliwal JS, Ceizar M, et al. 2016. Knockout of *Atg5* delays the maturation and reduces the survival of adult-generated neurons in the hippocampus. *Cell Death & Disease*, **7**(3): e2127.

Yamano K, Youle RJ. 2020. Two different axes CALCOCO2-RB1CC1 and OPTN-ATG9A initiate PRKN-mediated mitophagy. *Autophagy*, **16**(11): 2105–2107.

Yang JS, Chen XL, Xu HL. 2021. SQSTM1/p62 droplet -mediated autophagosome formation: insights into Huntington disease. *Autophagy*, **17**(10): 3256–3259.

Yang Y, Zhu YF, Zhou S, et al. 2022. TRIM27 cooperates with STK38L to inhibit ULK1-mediated autophagy and promote tumorigenesis. *The EMBO Journal*, **41**(14): e109777.

Yeo SK, Wang CR, Guan JL. 2020. Role of FIP200 in inflammatory processes beyond its canonical autophagy function. *Biochemical Society Transactions*, **48**(4): 1599–1607.

Zhao CM, Deng W, Gage FH. 2008. Mechanisms and functional implications of adult neurogenesis. *Cell*, **132**(4): 645–660.

Zheng XH, Wang WW, Liu RZ, et al. 2012. Effect of p62 on tau hyperphosphorylation in a rat model of Alzheimer's disease. *Neural Regeneration Research*, **7**(17): 1304–1311.

Zhou ZX, Liu JP, Fu T, et al. 2021. Phosphorylation regulates the binding of autophagy receptors to FIP200 Claw domain for selective autophagy initiation. *Nature Communications*, **12**(1): 1570.